Stability-superconductivity map for compressed Na-intercalated graphite

Shashi B. Mishra,* Edan T. Marcial, Suryakanti Debata, Aleksey N. Kolmogorov,† and Elena R. Margine‡
Department of Physics, Applied Physics and Astronomy, Binghamton University-SUNY, Binghamton, New York 13902, USA

(Received 16 July 2024; revised 1 October 2024; accepted 29 October 2024; published 13 November 2024)

A recent *ab initio* investigation of Na-C binary compounds under moderate pressures has uncovered a possible stable NaC_4 superconductor with an estimated critical temperature up to 41 K. We revisit this promising binary system by performing a more focused exploration of Na-intercalated graphite configurations, assessing the sensitivity of their thermodynamic stability to density functional approximations at different (T, P) conditions, and examining their superconducting properties with the Migdal-Eliashberg formalism. The combinatorial screening of possible Na arrangements reveals additional stable stoichiometries, *i.e.*, Na_3C_{10}, NaC_8, NaC_{10}, and NaC_{12}, that redefine the previously proposed convex hulls for pressures up to 10 GPa. The evaluation of formation enthalpies with different van der Waals functionals indicates that the proposed compounds might not be thermodynamically stable at zero temperature but some of them could stabilize due to the vibrational entropy or form via cold compression if graphite is used as a starting material. Our more rigorous modeling of the electron-phonon coupling in NaC_4 confirms the material's potential for high-temperature superconductivity, with a critical temperature reaching 48 K at 10 GPa, and reveals a well-defined two-gap structure unusual for an electron-doped compound. By tracking the position of the intercalant nearly free electron states with respect to the Fermi level in viable Na-C compounds, we map out the range of pressures and compositions needed for strong electron-phonon coupling and identify Na_3C_{10} as an equally promising superconductor.

DOI: 10.1103/PhysRevB.110.174508

I. INTRODUCTION

Carbon-based materials offer a rich playground in the quest for thermodynamically stable superconductors at ambient and low pressure [1–7]. Graphite intercalation compounds (GICs) [8], in particular, have been known to superconduct since the mid 1960s when superconductivity below 1 K was discovered in graphite intercalated with alkali metals (AC_8 with A = K, Rb, and Cs) [9]. Since then, considerable efforts have been made to find superconductivity in GICs at elevated temperatures, and the search has been focused on increasing the charge transfer from the intercalant atoms to the host graphene sheets by varying the stoichiometry and the intercalant type. To date, YbC_6 and CaC_6 with critical temperature (T_c) values of 6.5 K and 11.5 K stand as the highest temperature superconductors in this class under ambient conditions [10,11]. Superconductivity has also been induced or enhanced by applying external pressure. For instance, LiC_2 and NaC_2 become superconductors with $T_c = 1.9$ K at 3.3 GPa [12] and $T_c = 5.0$ K at 3.5 GPa [13], while in CaC_6 a maximum value of 15.1 K is reached at 7.5 GPa [14].

Recently, an *ab initio* evolutionary structure search in the Na-C system has identified a new GIC at the 1:4 composition [15]. The NaC_4 phase with the oS20 Pearson symbol and *Cmcm* symmetry [Fig. 1(c)] was predicted to stabilize above 8.9 GPa and have a maximum T_c of 41.2 K at 5 GPa. While this work has shown that the electron-phonon (e-ph) coupling is strong enough to yield a T_c above the record 39 K value in MgB_2 based on the Allen-Dynes modified McMillan formula [16,17], the nature of the superconducting gap has not been investigated.

Our present study reexamines the stability and superconductivity of Na-C candidate materials under pressures up to 10 GPa. Further exploration of the vast configuration space was motivated by the well-known difficulty of locating thermodynamically stable compounds even with the most advanced structure optimization methods [18–21]. For instance, our unconstrained evolutionary searches yielded a number of new complex crystal structures that have either been confirmed experimentally [22–24] or inspired the creation of more stable derivatives based on the identified favorable motifs [25–29]. In the latest investigation of layered metal borocarbides, we generated viable quaternary phases via systematic screening of possible metal decorations within ideal or modified honeycomb frameworks [29]. Application of this strategy to Na-C in the present work resulted in a significant revision of the previously proposed ground states. The updated set at 10 GPa contains large-sized oP104-Na_3C_{10}, oP18-NaC_8, oS44-NaC_{10}, and hP13-NaC_{12} phases that make mP12-NaC_2 metastable and oS20-NaC_4 marginally stable.

Importantly, we demonstrate that the global stability of these van der Waals solids is very sensitive to the treatment of the dispersive interactions. While the Na-C are thermodynamically stable in the optB88-vdW approximation of the nonlocal density functional [31], as was shown in Ref. [15], they have positive formation enthalpies in our optB86b-vdW [32] calculations. Fortunately, the inclusion of vibrational entropy brings them closer to stability and makes Na_3C_{10} a true ground state at room temperature. Moreover,

*Contact author: mshashi125@gmail.com
†Contact author: kolmogorov@binghamton.edu
‡Contact author: rmargine@binghamton.edu

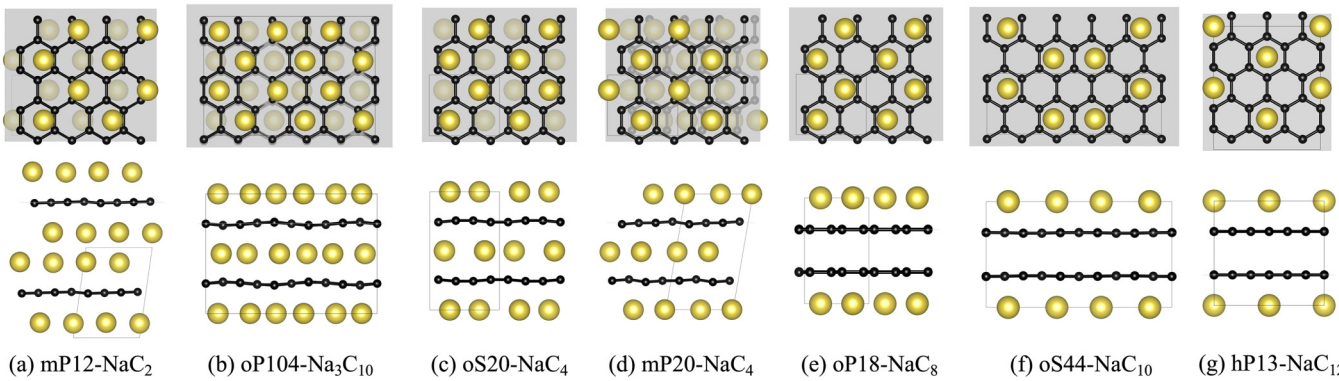

(a) mP12-NaC_2 (b) oP104-Na_3C_{10} (c) oS20-NaC_4 (d) mP20-NaC_4 (e) oP18-NaC_8 (f) oS44-NaC_{10} (g) hP13-NaC_{12}

FIG. 1. Select high-pressure Na-C phases found to be viable in previous [15] (a), (c) and present (b), (d), (e)–(g) *ab initio* studies. The top and side views show the corresponding distributions of Na (large yellow spheres) intercalated between C honeycomb layers (small black spheres). The figures were generated with VESTA [30].

we argue that the feasibility of obtaining the binary layered intercalated compounds should be evaluated with respect to graphite rather than diamond, provided that the synthesis starts with the former material and the (T, P) conditions are kept sufficiently low to avoid the sp^2 to sp^3 transformation. When referenced to the layered carbon polymorph, the Na-intercalated variants have negative formation Gibbs free energies.

Finally, we probe the proposed materials for superconducting properties. We analyze the position of the intercalant nearly free electron states across different phases and pressures to establish conditions needed for strong e-ph coupling. According to the constructed composition-pressure map, Na_3C_{10} compound with a complex structure has promise to be a high-T_c superconductor. We further study oS20-NaC_4 at 10 GPa using the fully anisotropic Migdal-Eliashberg (aME) formalism [33–35]. The aME method has been demonstrated to yield significantly higher estimates of the critical temperature, by a factor of two to three, in related layered conventional superconductors, *e.g.*, metal borides and borocarbides [33,36–41]. We calculate the momentum dependence of the e-ph coupling and superconducting energy gap on the Fermi surface. Our aME calculations yield a T_c of 48 K, which is slightly larger than the estimate of 39 K obtained in the previous work using an isotropic treatment of the e-ph coupling [15].

II. METHODS

We examined the stability of the Na-C phases with VASP [42] using projector augmented wave potentials [43]. By default, the nonlocal van der Waals interactions were treated with the optB86b-vdW functional [32], but also checked with alternative optB88-vdW [31] and r^{2}SCAN+rVV10 [44,45] functionals. Dense Monckhorst-Pack k-point meshes with $\Delta k \sim 2\pi \times 0.025$ Å^{-1} and a plane-wave cutoff of 500 eV ensured numerical convergence to typically within 1 meV/atom. To systematically screen possible decorations of interlayer sites, we constructed supercells with up to 42 atoms by expanding the stoichiometric MgB_2 prototype and sequentially removing metal atoms. For detection and elimination of equivalent configurations, we relied on our radial distribution function fingerprint [24]. We calculated thermodynamic corrections due to the vibrational entropy using the finite displacement method implemented in PHONOPY [46], employing supercells sized between 52 and 128 atoms and applying 0.04 Å displacements within the harmonic approximation. Full structural information for select phases is provided in the form of CIF files in Supplemental Material [47].

For calculating properties related to superconductivity, we employed the QUANTUM ESPRESSO (QE) package [48] with the optB86b-vdW functional [32,49,50] and optimized norm-conserving Vanderbilt pseudopotentials (ONCVPSP) [51] from the Pseudo Dojo library [52] generated with the relativistic Perdew-Burke-Ernzerhof parametrization [53]. We used a plane-wave cutoff of 100 Ry, a Methfessel-Paxton smearing [54] value of 0.02 Ry, and Γ-centered k-grids of $12 \times 12 \times 8$ for mP12-NaC_2, $12 \times 12 \times 8$ for oS52-Na_3C_{10}, $6 \times 6 \times 4$ for oP104-Na_3C_{10}, $16 \times 16 \times 16$ for oS20-NaC_4, $12 \times 12 \times 6$ for mP20-NaC_4, $6 \times 4 \times 5$ for oP18-NaC_8, $12 \times 12 \times 12$ for oS44-NaC_{10}, and $12 \times 12 \times 8$ for mP12-NaC_{12} to describe the electronic structure. The lattice parameters and atomic positions were relaxed until the total enthalpy was converged within 10^{-6} Ry and the maximum force on each atom was less than 10^{-4} Ry/Å. The dynamical matrices and the linear variation of the self-consistent potential were calculated within density-functional perturbation theory [55] on q-meshes of $3 \times 3 \times 2$ for mP12-NaC_2, $3 \times 3 \times 2$ for oS52-Na_3C_{10}, $1 \times 1 \times 1$ for oP104-Na_3C_{10}, $4 \times 4 \times 4$ for oS20-NaC_4, $4 \times 4 \times 2$ for mP20-NaC_4, $3 \times 2 \times 2$ for oP18-NaC_8, $3 \times 3 \times 3$ for oS44-NaC_{10}, and $4 \times 4 \times 3$ for mP12-NaC_{12}.

To investigate e-ph interactions and superconducting properties of oS20-NaC_4 further, we employed the EPW code [33,34,56,57]. The electronic wavefunctions required for the Wannier interpolation [58–60] were obtained on a uniform Γ-centered $8 \times 8 \times 8$ k-grid. We used ten atom-centered orbitals to describe the electronic structure of oS20-NaC_4, with one s orbital for each Na atom and one p_z orbital for each C atom. The anisotropic Migdal-Eliashberg equations were solved on fine uniform $80 \times 80 \times 80$ k- and $40 \times 40 \times 40$ q-point grids, with an energy window of ±0.2 eV around the Fermi level and a Matsubara frequency cutoff of 1.0 eV. When solving the isotropic ME equations, the Dirac deltas of electrons and phonons were replaced by Gaussians of width 50 meV and 0.3 meV, respectively.

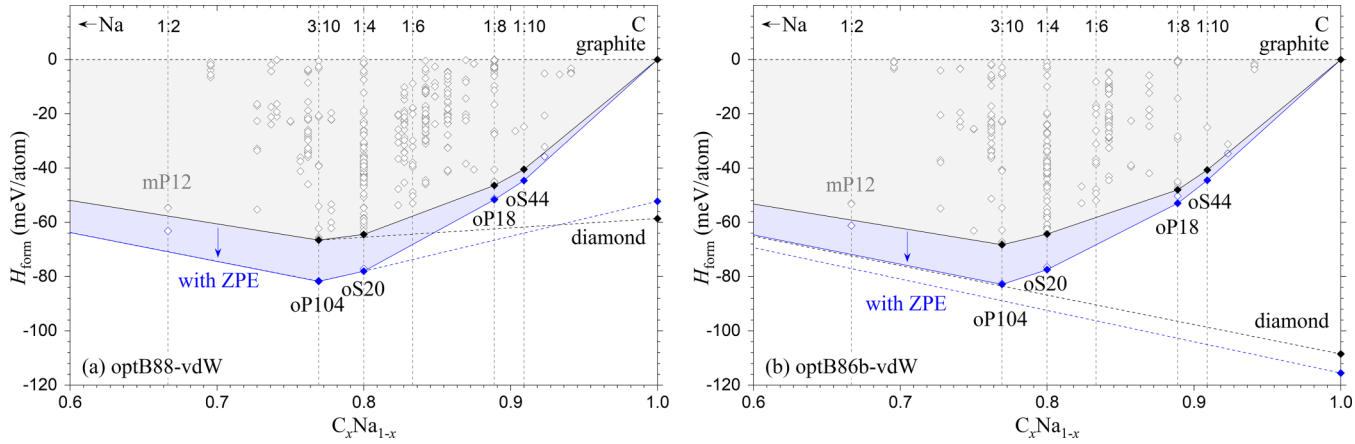

FIG. 2. Stability of Na-C phases at 10 GPa calculated with (a) the optB88-vdW functional or (b) the optB86b-vdW functional. The global (local) convex hulls are denoted with solid (dashed) lines. The formation enthalpies are shown with and without zero-point energy (ZPE) in blue and gray, respectively.

III. RESULTS AND DISCUSSIONS

A. Structure and stability of Na-C compounds

The global evolutionary searches by Hao *et al.* [15] provide an important baseline for viable morphologies in the Na-C binary up to 10 GPa. Namely, only graphite configurations intercalated with either one or two layers of Na appear to compete for thermodynamic stability across the composition range. We reproduce the negative formation enthalpy values evaluated with the optB88-vdW functional for the reported oS20-NaC_4 (−17.3 meV/atom) and mP12-NaC_2 (−15.9 meV/atom) phases relative to bcc-Na and diamond at 10 GPa. At the same time, we observe a high sensitivity of the results to phonon contributions and DFT approximations due to the starkly different bonding types displayed by the binary and reference phases. The inclusion of the zero-point energy (ZPE) alone shifts the values to −36.2 meV/atom and −28.4 meV/atom, respectively, and the vibrational entropy further stabilizes the intercalated compounds (see Fig. 2). The beneficial effect of temperature may be consequential because the formation enthalpies calculated in the optB86b-vdW approximation are positive, at 28.2 meV/atom and 23.7 meV/atom and the formation Gibbs free energies turn negative only at about 600 K. Considering the wide range of enthalpy values of graphite relative to diamond, 59, 88, and 116 meV/atom produced by the optB88-vdW, r^{2}SCAN+rVV10, and optB86b-vdW functionals, respectively, it is evident that the systematic errors are too large to make a definitive conclusion about the global stability of the Na-C intercalated phases.

Fortunately, the diamond reference is likely irrelevant if graphite is used as the starting material in the synthesis of the proposed binary compounds and the sample is not heated to high temperatures required to induce the sp^2 to sp^3 rebonding. According to the comprehensive review of extensive experimental work on carbon [61], the first signs of a structural phase transition in graphite under standard quasihydrostatic catalyst-free conditions at room temperature appear at 14-17 GPa. Measurements of electrical, optical, X-ray diffraction, and Raman response along with *ab initio* simulations indicate that the resulting cold compressed graphite features an sp^3-bonded morphology that reverts to the original state upon pressure release. Full irreversible transition to cubic or hexagonal diamond requires heating the sample to high temperatures, typically above 2,000 K at 15 GPa, or applying shear stress. The findings highlight the defining role of kinetics in the evolution of the covalently bonded framework under such moderate pressures. The increase in the interlayer spacing and the transfer of the negative charge to the C layers caused by Na intercalation may affect the kinetic barriers but are not expected to appreciably facilitate the rebonding in the targeted (T, P) range. Therefore, we find it more appropriate to define the synthesizability of the GICs with respect to bcc-Na and graphite rather than diamond not just up to 5 GPa where graphite is thermodynamically stable according to the optB88-vdW results at 0 K [15] (up to 2 GPa in our optB86b-vdW calculations) but up to at least 10 GPa. Figure 2 shows that the two proposed phases are indeed thermodynamically favorable with respect to the C layered polymorph, and the relative enthalpies agree well in the optB86b-vdW and optB88-vdW approximations due to the similarity of the elemental and binary morphologies.

Our screening of larger-sized intercalated structures offers further insight into what phases may form under pressure in this binary system. Starting with 14 different supercells of the MgB_2 or mP12-NaC_2 prototypes, we generated ∼750 unique Na_xC_2 configurations and fully optimized them at 10 GPa with both optB88-vdW and optB86b-vdW functionals to construct the convex hulls in Fig. 2 (the common ground states in the two approximations were also evaluated with the r^{2}SCAN+rVV10 functional). The considered phases had hexagonal (7%), orthorhombic (48%), monoclinic (38%), or trigonal (7%) unit cells with up to 52 atoms at 35 compositions below 1:2.

At the 1:4 stoichiometry corresponding to the previously proposed oS20 ground state, we find an alternative mP20 structure that is nearly degenerate in Gibbs free energy with oS20 in both optB86b-vdW and optB88-vdW calculations (see Figs. S1 and S2 [47]). The two phases have fairly uniform

metal decorations but the monoclinic variant features a pronounced interlayer shift that positions Na atoms near hexagon centers in one of the two sandwiching C layers [Figs. 1(c) and 1(d)]. The structural frustration with respect to sheer in these and other examined Na-C phases results in soft phonon modes that are difficult to converge.

The dominant compound at 10 GPa actually occurs at an unusual 3:10 composition in all considered vdW approximations (Figs. 2 and S3 [47]). The best oS52 structure with the *Cmcm* symmetry in the generated pool had multiple imaginary modes across the Brillouin zone (see Fig. S5 [47]). General strategies to deal with dynamically unstable structures include (i) checking convergence criteria to ensure that the structure indeed has imaginary frequencies [62–64]; (ii) following eigenvector(s) in the search for nearby local minima [25,62,65,66]; and (iii) considering anharmonic corrections to stabilize the structure at finite temperatures [62,67–70]. We checked that several phonon modes remain imaginary in our VASP calculations upon further structural relaxation (with residual forces below 0.01 eV/Å), increase of the k-point density (to $6 \times 6 \times 6$ in the $2 \times 2 \times 1$ 104-atom supercell), or change of the displacement value (0.04 Å or 0.10 Å). We proceeded with the generation of distorted derivatives by displacing atoms along selected eigenvectors in conventional (super)cells and constructed alternative phases, oS52 ($C222_1$) and oP104 ($P2_12_12_1$), with essentially identical enthalpies (within 0.1 meV/atom). In contrast to our previous successful identification of several local minima in CaB_6 by considering all possible combinations of imaginary eigenvectors at two high-symmetry points [25], the two derived Na_3C_{10} polymorphs also displayed several branches with imaginary frequencies (Figs. S6 and S7 [47]). To illustrate the particular challenge of finding a dynamically stable structure in this case, we plot the enthalpy profiles along a Γ-point soft-mode eigenvector representing the collective shear of the C layers in several phases (Fig. 4). The reason behind the much smaller enthalpy variation in the Na-C phases compared to that in graphite is the near 50% increase in the interlayer spacing that exponentially reduces the corrugation arising from the overlap of the C-p_z orbitals [71]. The resulting barriers in these GICs appear to be defined by the relative Na and C distributions in the neighboring layers. Since the Na atoms are not in perfect registry with the honeycomb lattice in either oS20-NaC_4 or oP104-Na_3C_{10} (*e.g.*, only a third of them reside above and below the C hexagon centers in the latter phase), the lack of short-period commensuration leads to the particularly smooth potential energy surfaces [72,73], and one can think of the materials as bearings with incompressible sheets sliding between large metal ion spheres. These observations help explain the slight differences between frozen phonon and linear response results (Figs. S7 and S8(b) [47]), as the choice of the displacement value can significantly affect the evaluation of force constants. Therefore, it is unlikely that either the creation of larger supercells or the inclusion of anharmonic effects would provide a definitive answer as to whether the layered Na-C phases can be represented with well-defined dynamically stable structures [69]. Domain formation or stacking disorder could be inherent features in these binary compounds, as was predicted in the related LiB material [74,75] and supported with XRD measurements [76]. For these reasons, we use the slightly favored oS20 and oP104 unit cells as representative models of the frustrated NaC_4 and Na_3C_{10} compounds, respectively, in the thermodynamic stability analysis but check the robustness of our superconductivity predictions by examining the additional closely related polymorphs.

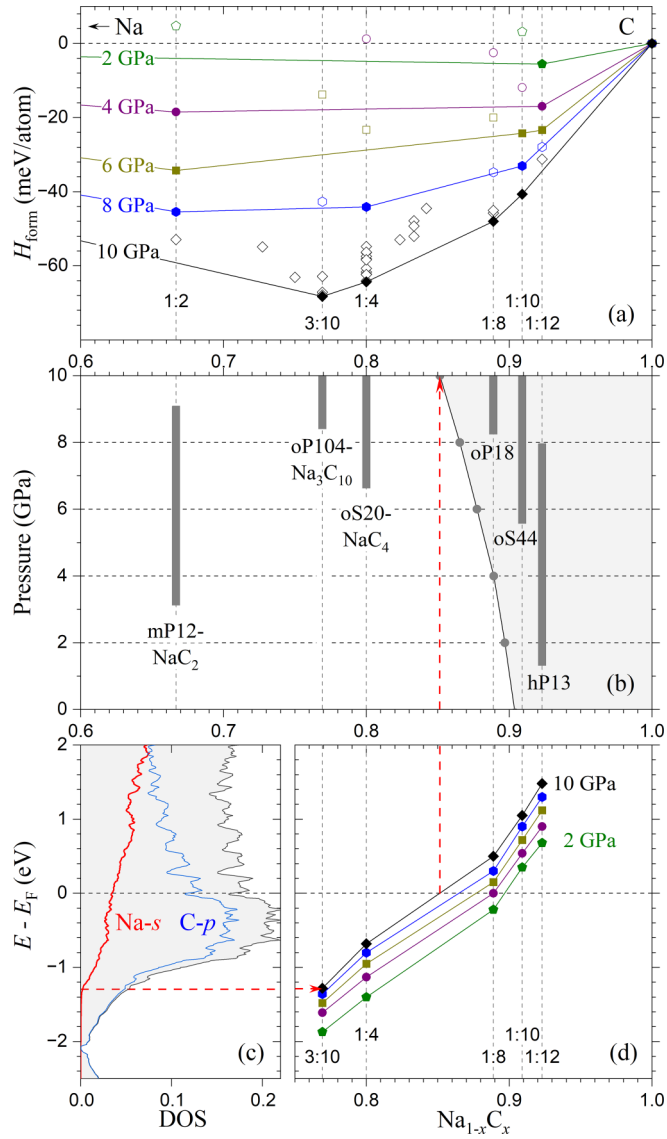

FIG. 3. Stability and electronic properties of $Na_{1-x}C_x$ compounds calculated with the optB86b-vdW functional. (a) Convex hulls with respect to bcc-Na and graphite at 2–10 GPa. (b) Stability ranges of the stable Na-C phases. The shaded area marks the (x, P) phase space in which Na-C materials are not expected to have electron-doped Na-*s* states important for superconductivity. (c) The density of states in oP104-Na_3C_{10}. The dashed red line shows the bottom of the Na-*s* states. (d) Position of the Na-*s* band edge for the intercalated Na-C compounds at 2−10 GPa. The dashed red line marks an approximate composition at which the Na-*s* band edge is expected to align with E_F at 10 GPa.

The oP104-Na_3C_{10} destabilizes the proposed double-layer mP12-NaC_2 phase at 10 GPa but leaves room for possible GICs at the low-Na composition end, such as NaC_8 and NaC_{10}. Figures 1(e) and 1(f) illustrate that the most favored configurations feature nearly flat C layers and Na

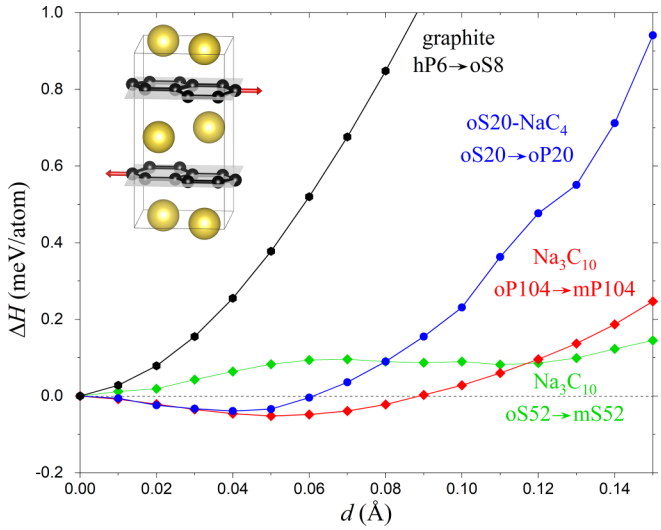

FIG. 4. Enthalpy change at 10 GPa along an optical phonon mode eigenvector that shears carbon layers. For each displacement value d, the neighboring C layers are shifted along C-C bonds in the opposite directions, with one C atom per layer fixed and all other structural parameters fully optimized. The corresponding changes in symmetry are $P6_3/mmc$ to $Cmcm$ (graphite), $Cmcm$ to $Pca2_1$ (oS20-NaC_4), $P2_12_12_1$ to $P2_1$ (oP104-Na_3C_{10}), and $Cmcm$ to $P2$ (oS52-Na_3C_{10}).

intercalating every other gallery, known as stage-two GICs. The lower Na concentration allows the metal sublattice to find a better balance between even distribution and registry with the honeycomb lattice. Consequently, oP18-NaC_8 and oS44-NaC_{10} are found to be dynamically stable [see Figs. 6(f) and 6(g)].

The resulting local convex hull (relative to graphite) at 0 K and 10 GPa is defined by four phases at the 3:10, 1:4, 1:8, and 1:10 compositions in all optB86b-vdW, optB88-vdW, and r^{2}SCAN+rVV10 approximations (Figs. 2 and S3 [47]). The set of ground states under 10 GPa compression remains unchanged at elevated temperatures once the vibrational entropy is included (Figs. S1 and S2 [47]), while transition pressures evaluated for select phases at 600 K instead of zero K shift by −0.8 GPa for oP104-Na_3C_{10}, −1.5 GPa for oS20-NaC_4, and 0.7 GPa for oP18-NaC_8. Interestingly, oP104-Na_3C_{10} is the only intercalated phase that is globally stable at room temperature in both DFT treatments (Fig. 2). To probe what GICs could be stable in the 1−10 GPa range, we reoptimized relevant phases at specific pressures, examined their relative enthalpies (Fig. S4 [47]), and constructed corresponding local convex hulls at 0 K (Fig. 3(a)). The first material to stabilize under compression is a stage-two hP13-NaC_{12} GIC derived from the $\sqrt{3} \times \sqrt{3} \times 2$ supercell of MgB_2. mP12-NaC_2 may indeed form just above 3 GPa (a related LiB compound with double metal layers has been synthesized via cold compression above 23 GPa [76]). The four proposed materials between the 3:10 and 1:10 ratios require higher pressures to be viable [see Fig. 3(b)]. Our comparison of the optB86b-vdW and optB88-vdW results in Fig. S4 [47] shows that the phase transition pressure estimates in the two approximations agree to within 1 GPa.

B. Electronic, vibrational, and superconducting properties of Na-C phases

To screen the Na-C binary system for possible high-T_c superconductivity, we investigated the electronic, vibrational, and superconducting properties in the proposed set of intercalated phases, mP12-NaC_2, oS52 (oP104)-Na_3C_{10}, oS20 (mP20)-NaC_4, oP18-NaC_8, oS44-NaC_{10}, and hP13-NaC_{12}, at pressures up to 10 GPa. First, we examined the response of the intercalant Na-s states to composition and pressure to determine conditions under which the band crosses the Fermi level (E_F). The presence of the partially occupied nearly free electron (NFE) states has been linked to superconductivity in several layered compounds (*e.g.*, CaC_6 and YbC_6 GICs [77–79], bilayer C_6CaC_6 [80,81], monolayer LiC_6 [82,83], and LiB [39,84]). The strong interaction of this band with the surrounding lattice has been rationalized as a response to both quantum confinement and electrostatic effects [82,85,86].

Our electronic band structure and density of states (DOS) calculations show that only compounds at the 1:2, 3:10, and 10:4 compositions have partially occupied Na-s states in the considered pressure range [see Figs. 3(c), 3(d), and 5]. Among them, mP12-NaC_2 stands out as the only one with a 2D shape of the Na DOS around the Fermi level and with very little dependence of the band edge position on pressure (about −3.0 eV at 10 GPa). In contrast, just as in LiB [84], the Na DOS in the Na_3C_{10} and NaC_4 phases has a 3D profile, and compression from 2 GPa to 10 GPa raises these NFE states by about 0.6 eV. Fortunately, the band edge remains at −1.3 eV and −0.7 eV below the Fermi level in the two respective Na-C compounds at 10 GPa as shown in Fig. 3(d). As in CaC_6 [77,87], the dominant contribution to the DOS at the Fermi level ($N(E_F)$) comes from the antibonding C-π^* states. Another important characteristic is the close resemblance of the overall DOS shape in the oS52 (oP104)-Na_3C_{10} and oS20 (mP20)-NaC_4 phases at the 3:10 and 1:4 compositions, suggesting that they may have similar superconducting properties.

Decreasing the metal concentration has a strong effect on the position of the NFE band. The data in Figs. 3(d) and 5 illustrate that while the stage-two oP18-NaC_8, oS44-NaC_{10}, and hP13-NaC_{12} are still metallic, none of them features the Na-s states at the Fermi level in the corresponding regions of thermodynamic stability. For instance, this band would be partially occupied in oP18-NaC_8 below 4 GPa but the phase requires over 8 GPa to break the convex hull [see Fig. 3(b)]. Since the three Na-poor GICs have similar DOS shapes and can be modeled with a rigid-band approximation, $N(E_F)$ is defined primarily by the amount of available charge to fill the C-π^* states and happens to decrease with the Na content. Figures 5(f)–5(h) and Table I demonstrate that the resulting $N(E_F)$ values in two of the three phases are significantly lower than those in the considered stage-one GICs.

To construct an approximate $x(P)$ boundary between $Na_{1-x}C_x$ compounds with and without populated Na-s states, we estimated the critical concentrations x by linear interpolations at every 2 GPa pressure (the dashed red line across panels (b) and (d) of Fig. 3 illustrates the determination of the point at 10 GPa). The near-linear shift of the critical

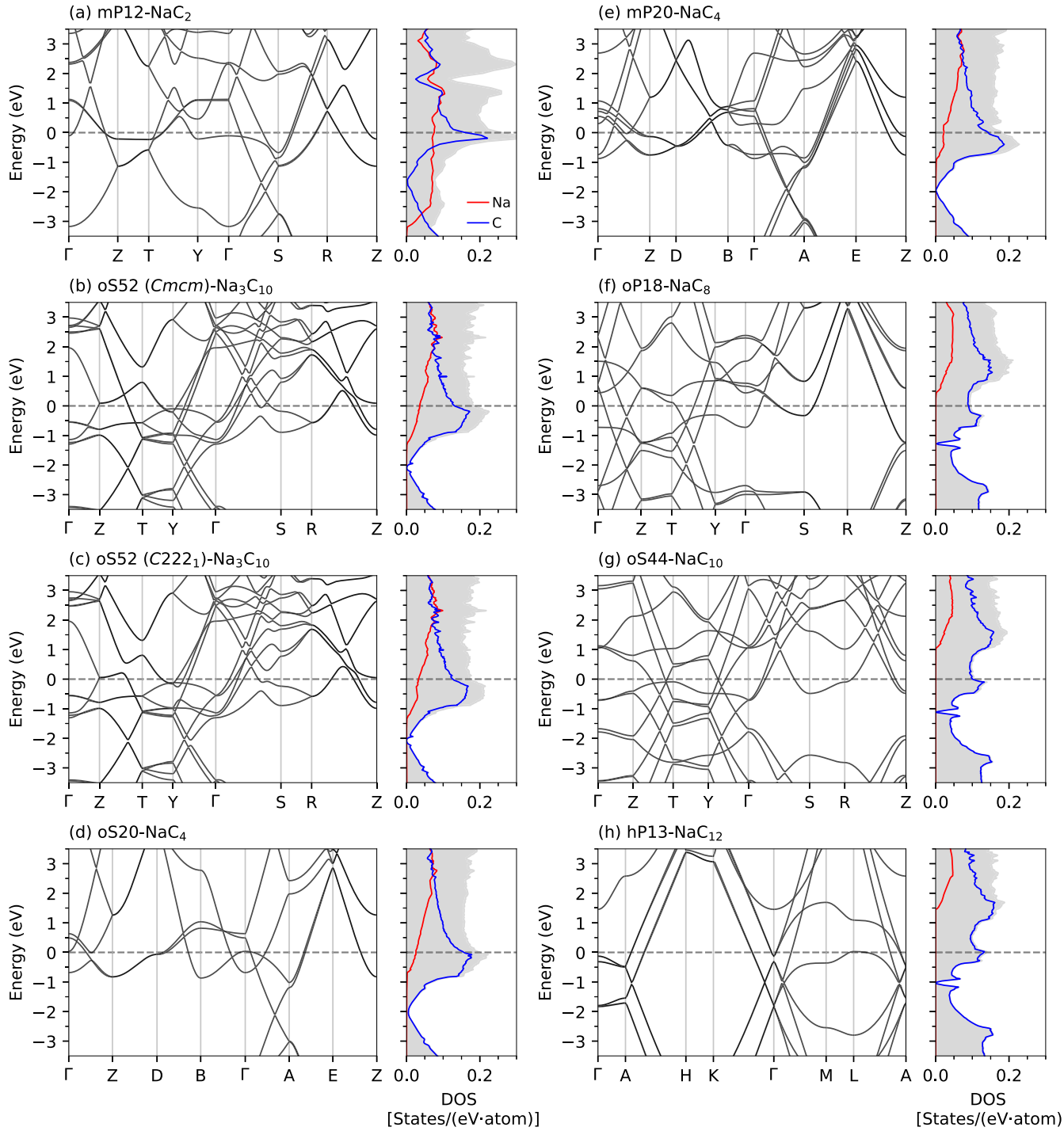

FIG. 5. Electronic band structures and density of states (DOS) calculated with Quantum ESPRESSO at 10 GPa for (a) mP12-NaC_2, (b) oS52 (*Cmcm*)-Na_3C_{10}, (c) oS52 ($C222_1$)-Na_3C_{10}, (d) oS20-NaC_4, (e) mP20-NaC_4, (f) oP18-NaC_8, (g) oS44-NaC_{10}, and (h) hP13-NaC_{12}.

compositions with pressure found for the phases with different symmetries suggests little sensitivity of the Na-*s* energies to the particular decoration of the metal sites as long as the arrangements within galleries are fairly uniform (see Fig. 1). The resulting shaded area in Fig. 3(b), extrapolated down to the ambient pressure, marks the $x(P)$ region in which Na-C phases are not expected to have superconductivity arising primarily from the strong coupling to the intercalant states.

To check the validity of this observation, we looked at the vibrational and superconducting properties for this set of materials with the QE package. Similar to CaC_6 and several other GICs [77,88,89], the phonon dispersion can be divided into three regions (see Figs. 6, S8, and S11 [47]): a low-frequency region composed of mostly in-plane Na_{xy} vibrations mixed with out-of-plane C_z vibrations (<30 meV), an intermediate frequency region dominated by out-of-plane C_z and Na_z vibrations (30−100 meV), and a high-frequency

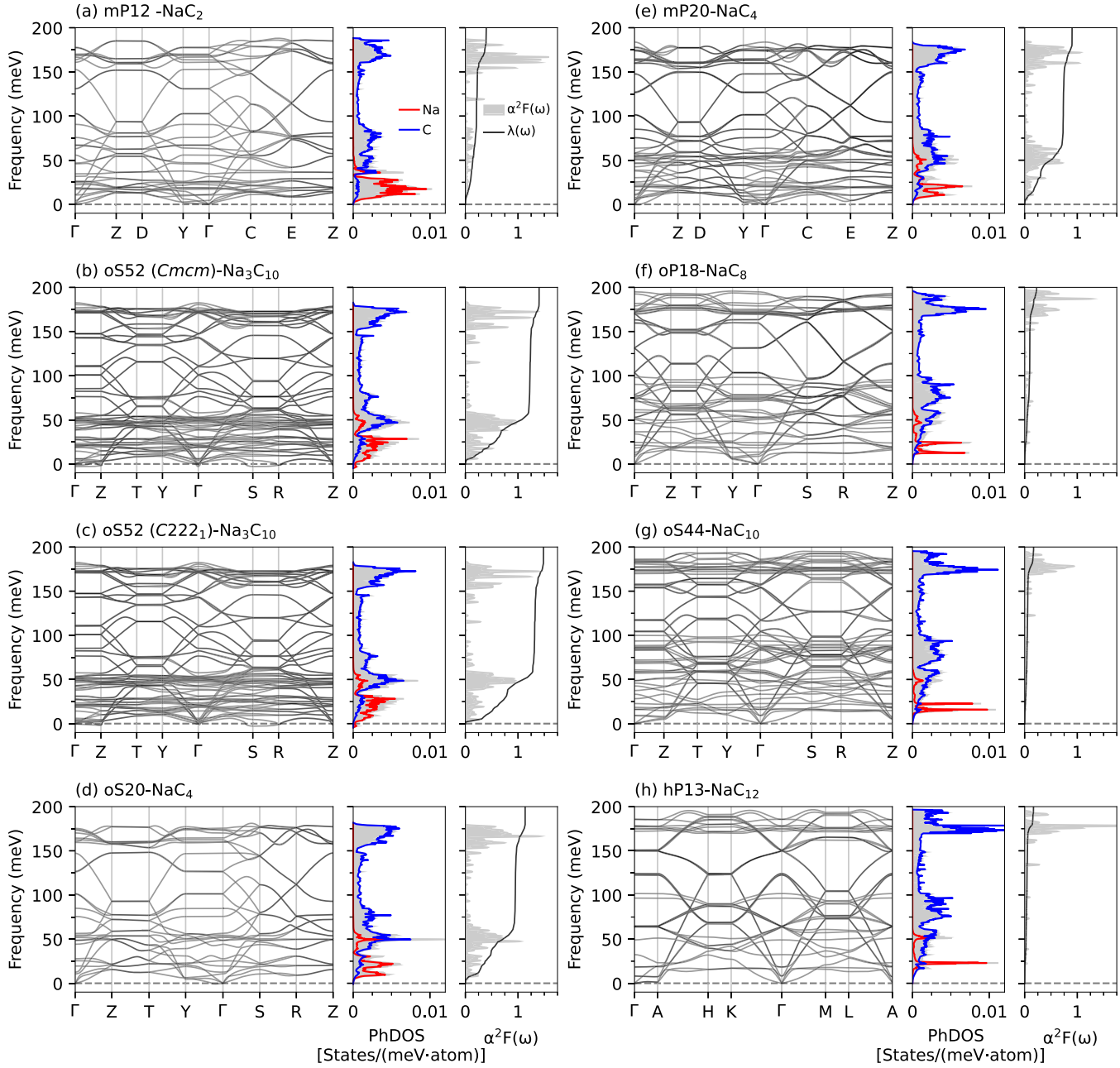

FIG. 6. Phonon dispersion, phonon density of states (PhDOS), Eliashberg spectral function $\alpha^2F(\omega)$, and integrated electron-phonon coupling strength λ^{QE} calculated with Quantum ESPRESSO at 10 GPa for (a) mP12-NaC_2, (b) oS52 ($Cmcm$)-Na_3C_{10}, (c) oS52 ($C222_1$)-Na_3C_{10}, (d) oS20-NaC_4, (e) mP20-NaC_4, (f) oP18-NaC_8, (g) oS44-NaC_{10}, and (h) hP13-NaC_{12}. The $\alpha^2F(\omega)$ and λ^{QE} for Na_3C_{10} structures are estimated by neglecting the imaginary phonon frequencies.

region of in-plane C_{xy} vibrations (>100 meV). The superconducting T_c was estimated using the Allen-Dynes modified McMillan formula [16,17] with a Coulomb potential $\mu^* = 0.1$. We denote the e-ph coupling strength and the critical temperature obtained with QE as λ^{QE} and T_c^{QE}, respectively, to differentiate them from the EPW values discussed in the next section. Table I summarizes λ^{QE} and T_c^{QE} for all the $Na_{1-x}C_x$ compounds.

Unsurprisingly, the three phases in the gray region of Fig. 3(b) probed within their respective stability regions oP18-NaC_8 at 10 GPa, oS44-NaC_{10} at 10 GPa, and hP13-NaC_{12} at 5 GPa, were found to have low λ^{QE} of 0.23, 0.17, and 0.18, respectively, with no measurable T_c^{QE} values. Upon examination of the Eliashberg spectral function $\alpha^2F(\omega)$ and the cumulative e-ph coupling strength $\lambda(\omega)$ plotted in Fig. 6, we conclude that the underlying factor determining the reduced λ^{QE} values in these cases is the absence of e-ph coupling for the Na and out-of-plane C_z phonon modes from the low- and intermediate-frequency region below 100 meV.

For oS20-NaC_4 and mP12-NaC_2 at 10 GPa, our calculations produced λ^{QE} values of 1.13 and 0.40, with corresponding T_c^{QE} values of 33.5 K and 3.0 K, consistent with Ref. [15]. We find that the low- and intermediate-frequency phonons play a key role in achieving a high e-ph

TABLE I. Properties of $Na_{1-x}C_x$ phases: The average interlayer distance d_{inter}, the density of states at the Fermi level $N(E_F)$, the nearly-free energy (NFE) band occupation, the logarithmic average phonon frequency ω_{log}, the total electron-phonon coupling strength λ^{QE}, and the superconducting critical temperature T_c^{QE} with a Coulomb potential $\mu^* = 0.1$. Note that λ^{QE} and T_c^{QE} for oP104-Na_3C_{10} were obtained using phonon calculations for a single q-point (Γ).

Phase composition	Space group	Pearson symbol	Pressure (GPa)	d_{inter} (Å)	$N(E_F)$ (states/eV · atom)	NFE occupation	ω_{log} (meV)	λ^{QE}	T_c^{QE} (K)
NaC_2	$P2_1m$	mP12	10	6.81	0.261	Yes	64.1	0.40	3.0
Na_3C_{10}	$Cmcm$	oS52	10	4.22	0.191	Yes	30.4	1.40	37.5
Na_3C_{10}	$C222_1$	oS52	10	4.20	0.181	Yes	22.5	1.50	29.6
Na_3C_{10}	$P2_12_12_1$	oP104	10	4.26	0.176	Yes	30.8	1.43	39.1
NaC_4	$Cmcm$	oS20	10	4.23	0.199	Yes	34.6	1.13	33.5
NaC_4	$P2_1/m$	mP20	10	4.17	0.161	Yes	42.3	0.89	28.5
NaC_8	$Pmma$	oP18	10	4.21	0.066	No	97.8	0.23	–
NaC_{10}	$Cmcm$	oS44	10	4.17	0.085	No	108.8	0.17	–
NaC_{12}	$P6/mmm$	hP13	5	4.10	0.153	No	114.5	0.18	–
NaC_{12}	$P6/mmm$	hP13	10	4.10	0.141	No	120.9	0.17	–

coupling in oS20-NaC_4, and together they account for approximately 84% of the total $\lambda^{QE} = 1.13$. Moreover, the relative contributions of these two sets of modes are very similar, with the low and intermediate regions making up 40% and 44% of λ, respectively. Notably, the high-frequency in-plane C_{xy} modes exhibit a significantly smaller contribution of only about 16%. This behavior is similar to other GICs (*e.g.*, CaC_6, BaC_6, and SrC_6 [77,81,87,88]) and Ca-intercalated bilayer graphene [81], where the largest contribution to the e-ph coupling strength has been associated with the modes below 100 meV. While the coupling to these critical modes is present in mP12-NaC_2, their contribution is reduced by a factor of four compared to that in oS20-NaC_4, which leads to a drastic reduction in the e-ph coupling strength and the critical temperature. For the competing mP20-NaC_4 structure at the 1:4 composition, we find $\lambda^{QE} = 0.89$ and $T_c^{QE} = 28.5$ K. Comparison of Figs. 6(d) and 6(e) reveals that the in-plane C_{xy} vibrations in the high-frequency region above 100 meV have a nearly identical contribution to λ^{QE} in the two NaC_4 phases, and the difference in their total coupling strengths can be again attributed to the low- and intermediate-frequency phonons.

Finally, we investigated the superconducting properties of the three Na_3C_{10} structures. Since at the harmonic level the phonon dispersions exhibit two slightly imaginary modes with frequencies around -2.9 meV, the e-ph properties were computed by integrating only over the real frequency modes (see Figs. 6(b), 6(c), and S8(b) [47]), similar to what was done in recent studies [90,91] (note that the lower integration limit in QE is set to 2.5 meV and such modes would be ignored even if their frequencies were real but below this threshold). Importantly, the phonon DOS and the Eliashberg spectral functions results plotted in Fig. 6 show that the soft phonon modes below 10 meV corresponding to C layer shifts have insignificant contribution to the total coupling even in the dynamically stable NaC_4 phases and that the dominant parts of $30-50\%$ and $40-50\%$ in all considered 1:4 and 3:10 GICs come from the Na-based modes in the $0-30$ meV range and C-based modes in the $30-100$ meV range, respectively. The relatively high λ^{QE} (T_c^{QE}) values of 1.40 (37.5 K), 1.50 (29.6 K), and 1.43 (39.1 K) obtained at 10 GPa for the oS52 ($Cmcm$), oS52 ($C222_1$), and oP104 structural models indicate that Na_3C_{10} should be as good a superconductor as NaC_4. Hence, we believe that the conclusions drawn from our following in-depth analysis of the superconducting properties in oS20-NaC_4 with the anisotropic Migdal-Eliashberg formalism should be transferable to the neighboring Na_3C_{10} compound.

C. Superconducting properties of NaC_4 with the anisotropic Migdal-Eliashberg formalism

With the oS20-NaC_4 phase determined to stabilize above 6.5 GPa, we performed a more detailed examination of its properties at 10 GPa. More insight into the electronic structure can be obtained by analyzing the dispersion of oS20-NaC_4 with Na atoms removed (empty graphite-like C_4 structure, solid black lines) and the one with C atoms removed (empty Na metal structure, red dashed lines) depicted in Fig. S9(c) [47]. Comparing Figs. S9(a) and S9(c) [47], we can interpret the band structure of oS20-NaC_4 as a superposition of the C_4 and Na bands. To facilitate this comparison, the C and Na bands in Fig. S9(c) are shifted downward and upward by $\sim$2 eV, respectively, to match the Fermi level in oS20-NaC_4. Effectively, the relative shift is equivalent to a charge transfer from the Na atoms to the graphene layers. This can be clearly visualized from the charge density difference plot in Fig. S9(d), where the red and green lobes represent the charge accumulation and depletion regions around the C and Na atoms, respectively. Integrating the atomic-projected DOS, we extract the Löwdin charge for each atom. In oS20-NaC_4, we find a charge transfer of 0.21 electrons/C atom, whereas in CaC_6 each C atom only gains 0.11 electrons [77].

Figure S10 [47] illustrates the total and band-decomposed Fermi surface (FS). Comparison with the band structure in Fig. S9(a) reveals that the three bands crossing the Fermi level give rise to a multi-sheet FS structure. The FS sheets corresponding to band 1 (shown in blue) and band 2 (shown in green) exhibit 3D nested shapes and originate from the C-p_z states, as already pointed out in Ref. [15]. These nested regions surround two bean-shaped FS sheets (shown in red) centered around Γ of predominant Na-s character (band 3).

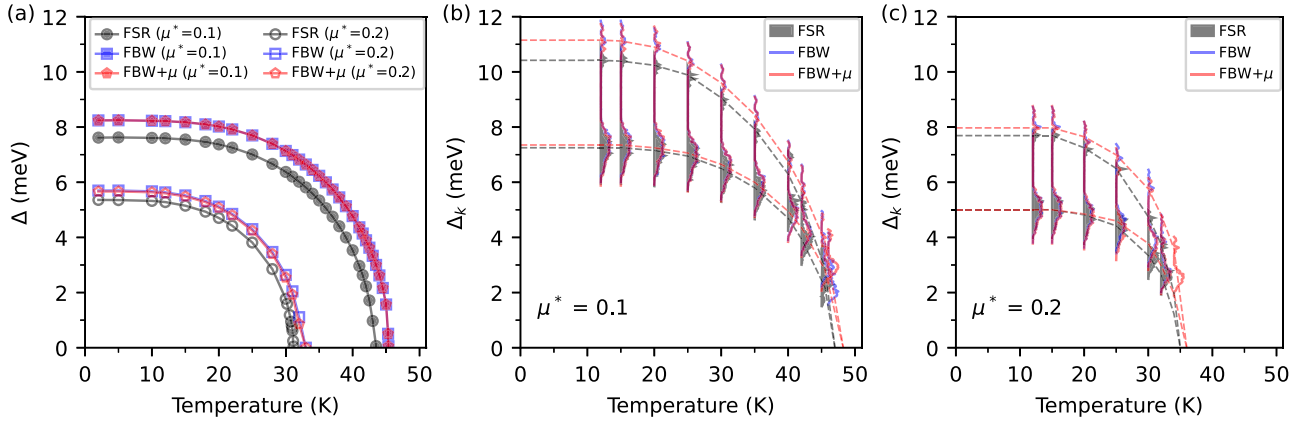

FIG. 7. Superconducting properties of oS20-NaC_4 at 10 GPa obtained with the FSR (gray), FBW (blue), and FBW+μ (red) approaches for $\mu^* = 0.1$ and 0.2. (a) Isotropic superconducting gap Δ as a function of temperature. (b) and (c) Energy distribution of the anisotropic superconducting gap $\Delta_{\boldsymbol{k}}$ as a function of temperature. The black dashed lines in (b) and (c) represent a guide for the eye highlighting the two superconducting gap distributions.

To investigate the e-ph interaction, we computed the isotropic Eliashberg spectral function $\alpha^2F(\omega)$ and the cumulative e-ph coupling strength $\lambda(\omega)$ with EPW (see Fig. S11(c) [47]). Consistent with our QE results, we find a high e-ph coupling strength $\lambda = 1.19$. The anisotropy in the e-ph coupling is quantified by evaluating the momentum-resolved $\lambda_{\boldsymbol{k}}$ as defined in Ref. [33]. Figure S12(a) [47] clearly displays two peaks in the distribution of $\lambda_{\boldsymbol{k}}$, with a sharp peak centered around 1 and a small peak centered around 3. To further analyze the origin of these peaks, the variation of $\lambda_{\boldsymbol{k}}$ on the Fermi surface is shown in Fig. S12(b) [47]. According to the color map, the first sharp peak originates from the nested FS regions, while the second smaller peak arises from the Γ-centered FS regions. In particular, by comparing with the band structure and the band decomposed FS plots in Figs. S9(a) and S10 [47], it becomes evident that the first peak arises from the coupling of the phonon modes with the C-π^* states (band 1 and band 2), while the second peak is mostly due to the intercalant Na-s states (band 3) with some contribution from the C-π^* states (band 2).

In order to determine the superconducting critical temperature, we solved the isotropic and anisotropic Migdal-Eliashberg equations [33,34]. Since the electronic DOS strongly peaks close to E_F, we examined the superconducting gap using both the Fermi surface restricted (FSR) and the full bandwidth (FBW) approaches [34,35]. In FSR, the DOS around E_F is assumed constant, whereas in FBW the full energy dependence of the DOS is considered, allowing the inclusion of e-ph scattering processes away from E_F. A recent study has demonstrated the importance of the FBW treatment in the high-pressure H_3S and the low-pressure $BaSiH_8$ superconductors, which exhibit distinct DOS features that deviate significantly from the constant-DOS assumption made in the FSR approximation [35]. For a detailed description of the FSR and FBW approaches and their implementation in the EPW code, please see Refs. [33–35,57].

Figure 7(a) shows the isotropic superconducting gap Δ as a function of temperature, calculated with the FSR, FBW, and FBW+μ methods using a Coulomb parameter $\mu^* = 0.1$ and 0.2. In the FBW+μ approach, the chemical potential is updated self-consistently as discussed in Ref. [35]. Our calculations yield T_c values of 43.5 (31.2) K and 45.5 (33.0) K, and a zero-temperature superconducting gap of 7.62 (5.36) meV and 8.24 (5.70) meV for FSR and FBW with $\mu^* = 0.1$ (0.2), respectively. Furthermore, the superconducting gap versus temperature curves for FBW and FBW+μ are basically identical, thus leading to the same T_c values. This can be understood as the Fermi level in oS20-NaC_4 lies slightly away from the van Hove singularity (vHS) peak, as shown in Fig. S9(b), and therefore the DOS with and without updating μ are very similar. For comparison, the commonly employed Allen-Dynes (AD) modified McMillan formula [16,17] and the machine-learned (ML) SISSO model [93] give T_c values of 34.9 (22.0) K and 43.3 (26.7) K for $\mu^* = 0.1$ (0.2), respectively, with the latter producing results that match very well our isotropic predictions.

Given the anisotropy found in $\lambda_{\boldsymbol{k}}$, we calculated the anisotropic superconducting gap $\Delta_{\boldsymbol{k}}$ as a function of temperature shown in Figs. 7(b) and 7(c). We find two distinct gaps with mean values $\Delta_1 = 7.25$ (5.00) meV and $\Delta_2 = 10.42$ (7.69) meV for $\mu^* = 0.1$ (0.2) in the zero-temperature limit using the FSR approach. For comparison, CaC_6 displays a continuum anisotropic gap without separation into distinct gaps [81,87,89]. The Δ_1 gap is highly anisotropic and varies over a wide energy range of 1.75 meV. In contrast, the Δ_2 gap is less pronounced (*i.e.*, fewer energy states contribute to this gap) and has a much narrower distribution of only 0.75 meV. The superconducting T_c is estimated to be 47.0 (35.0) K for $\mu^* = 0.1$ (0.2), about 8% (12%) higher than the isotropic FSR value. Application of the FBW and FBW+μ treatments only shifts slightly the gap distribution to higher energies while retaining the overall shape at each temperature. The resulting T_c using the two FBW approaches is estimated to be 48.2 (36.0) K with $\mu^* = 0.1$ (0.2). The T_c values obtained with different approaches are summarized in Table II.

Figure 8(a) shows the momentum-resolved superconducting gap $\Delta_{\boldsymbol{k}}$ on the FS at 12 K within the FSR approximation using $\mu^* = 0.1$. Comparing this with Fig. S12(b) [47], the regions of the FS with the lower gap $\Delta_1 = 7.35$ meV can

TABLE II. Properties of oS20-NaC_4 at 10 GPa: the density of states at the Fermi level $N(E_F)$, the logarithmic average phonon frequency ω_{log}, the electron-phonon coupling strength λ, the Coulomb parameter μ^*, and the superconducting critical temperature T_c. The T_c values are calculated using different methodologies: the semi-empirical Allen-Dynes (AD) formula, the machine-learned (ML) model, the isotropic and anisotropic Fermi surface restricted (FSR) approximation, and the isotropic and anisotropic full bandwidth implementation without (FBW) and with (FBW+μ) variation of the chemical potential μ.

$N(E_F)$	ω_{log}			Semi-empirical T_c (K)		Isotropic ME T_c (K)			Anisotropic ME T_c (K)		
(states/(eV · atom))	(meV)	λ	μ^*	AD	ML	FSR	FBW	FBW+μ	FSR	FBW	FBW+μ
0.19	33.9	1.19	0.1	34.9	43.3	43.5	45.5	45.5	47.0	48.2	48.2
			0.2	22.0	26.7	31.2	33.0	33.0	35.0	36.0	36.0

be associated with the C-π^* states (band 1 and band 2). In contrast, the upper gap $\Delta_2 = 10.60$ meV primarily arises from the Na-*s* states (band 3) with some contribution from the C-π^* states (band 2). Similarly, in CaC_6, the smallest and highest values of the smeared multi-gap structure have been associated with the C-π^* and Ca $-$ *s*, d_{z^2} states [87,89]. The two-gap structure of oS20-NaC_4 is also evident from the corresponding quasiparticle DOS plotted in Fig. 8(b).

Finally, we explored the effect of electron and hole doping on the T_c in the light of the vHS peak present in the DOS of oS20-NaC_4 near the Fermi level [see Fig. 9(a)]. Previous theoretical studies on H_3S have shown an enhancement in T_c when the Fermi level approaches the maximum of the vHS peak [35,94,95]. To investigate the dependence of T_c with doping, we shifted the Fermi level by $\Delta\varepsilon_F$ in the -0.2 eV to 0.1 eV range in increments of 0.05 eV, corresponding to changes in the electron number of $\sim$0.076. Figure 9(b) shows the T_c values obtained by solving the isotropic and anisotropic ME equations within the FSR and FBW approaches, and those obtained with the semi-empirical AD and ML formulas. Overall, all treatments produce a similar trend for the variation of T_c with doping. In particular, the T_c versus $\Delta\varepsilon_F$ curve obtained with the anisotropic approach resembles the shape dependence of the DOS, the T_c reaching a maximum value at $\Delta\varepsilon_F = -0.1$ eV when the Fermi level lies in very close proximity to the vHS peak. For comparison, the effect of doping on T_c is less pronounced when employing the isotropic ME treatment or the semi-empirical formulas, with the AD formula consistently underestimating the T_c values by about 7 K.

IV. SUMMARY

We have explored the stability and superconductivity of Na-intercalated graphite compounds under moderate pressures using *ab initio* methods. Through systematic screening, we identified new stable stoichiometries, Na_3C_{10}, NaC_8, NaC_{10}, and NaC_{12}, which redefine the previously established convex hulls up to 10 GPa. While some compounds may lack stability at zero temperature, they could be high-temperature ground states or form through cold compression of graphite. Our analysis of the nearly free electron states important for superconductivity in intercalated compounds narrows down the promising candidates to two. One of them, NaC_4 proposed previously by Hao *et al.* [15], has been re-analyzed within the anisotropic Migdal-Eliashberg theory and predicted to be a two-gap superconductor with a T_c of 48 K, 24% above the prior isotropic Eliashberg estimate. The other compound, Na_3C_{10} introduced in the present study, appears to be prone to interlayer shifts and may develop domain walls to become dynamically stable. According to our estimates, it should have T_c at least comparable to that in NaC_4 at 10 GPa. The *ab initio* findings reveal the Na-C system may host viable compounds with unexpectedly high T_c for electron-doped materials.

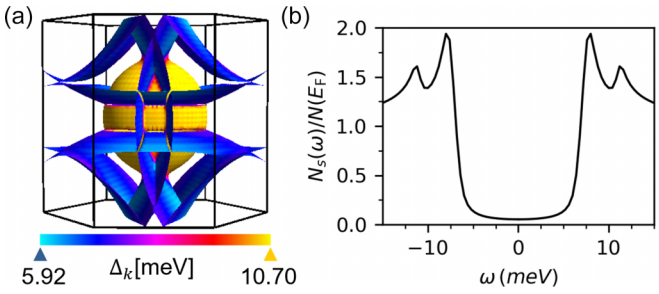

FIG. 8. (a) Momentum-resolved superconducting gap Δ_k on the Fermi surface generated with FermiSurfer [92], and (b) normalized quasiparticle DOS using the FSR approach with $\mu^* = 0.1$ for oS20-NaC_4 at 12 K and 10 GPa.

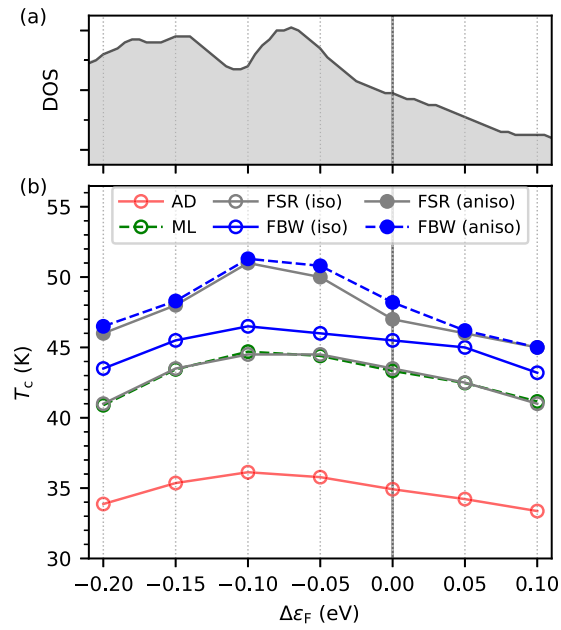

FIG. 9. (a) Total DOS in the energy range of -0.2 to 0.1 eV around the Fermi level, and (b) superconducting critical temperature T_c as a function of Fermi level shift $\Delta\varepsilon_F$ obtained with the AD formula, the ML model, and the isotropic and anisotropic ME equations in the FSR and FBW approaches with a $\mu^* = 0.1$ for oS20-NaC_4 at 10 GPa.

ACKNOWLEDGMENTS

S.B.M. and E.R.M. acknowledge support from the National Science Foundation (NSF) Award No. DMR-2035518. E.T.M. and A.N.K. acknowledge support from the NSF Award No. DMR-2320073. This study used the Frontera supercomputer at the Texas Advanced Computing Center through the Leadership Resource Allocation (LRAC) Award No. DMR22004. Frontera is made possible by NSF Award No. OAC-1818253 [96]. This study also used the Expanse system at the San Diego Supercomputer Center through allocation TG-DMR180071 from the Advanced Cyberinfrastructure Coordination Ecosystem: Services & Support (ACCESS) program [97], which is supported by NSF Grants No. 2138259, No. 2138286, No. 2138307, No. 2137603, and No. 2138296.

[1] R. A. Jishi and M. S. Dresselhaus, Superconductivity in graphite intercalation compounds, Phys. Rev. B **45**, 12465 (1992).

[2] E. Ekimov, V. Sidorov, E. Bauer, N. Mel'Nik, N. Curro, J. Thompson, and S. Stishov, Superconductivity in diamond, Nature (London) **428**, 542 (2004).

[3] H. Okazaki, T. Wakita, T. Muro, T. Nakamura, Y. Muraoka, T. Yokoya, S.-i. Kurihara, H. Kawarada, T. Oguchi, and Y. Takano, Signature of high Tc above 25 K in high quality superconducting diamond, Appl. Phys. Lett. **106**, 052601 (2015).

[4] S. Heguri, N. Kawade, T. Fujisawa, A. Yamaguchi, A. Sumiyama, K. Tanigaki, and M. Kobayashi, Superconductivity in the graphite intercalation compound BaC_6, Phys. Rev. Lett. **114**, 247201 (2015).

[5] H. Zhou, T. Xie, T. Taniguchi, K. Watanabe, and A. F. Young, Superconductivity in rhombohedral trilayer graphene, Nature (London) **598**, 434 (2021).

[6] A. Bhaumik, R. Sachan, S. Gupta, and J. Narayan, Discovery of high-temperature superconductivity ($T_c = 55$ K) in B-doped Q-Carbon, ACS Nano **11**, 11915 (2017).

[7] N. Emery, C. Hérold, J.-F. Marêché, and P. Lagrange, Synthesis and superconducting properties of CaC_6, Sci. Technol. Adv. Mater. **9**, 044102 (2008).

[8] M. Dresselhaus and G. Dresselhaus, Intercalation compounds of graphite, Adv. Phys. **30**, 139 (1981).

[9] N. B. Hannay, T. H. Geballe, B. T. Matthias, K. Andres, P. Schmidt, and D. MacNair, Superconductivity in graphitic compounds, Phys. Rev. Lett. **14**, 225 (1965).

[10] T. E. Weller, M. Ellerby, S. S. Saxena, R. P. Smith, and N. T. Skipper, Superconductivity in the intercalated graphite compounds C_6Yb and C_6Ca, Nat. Phys. **1**, 39 (2005).

[11] N. Emery, C. Hérold, M. d'Astuto, V. Garcia, C. Bellin, J. F. Marêché, P. Lagrange, and G. Loupias, Superconductivity of bulk CaC_6, Phys. Rev. Lett. **95**, 087003 (2005).

[12] I. Belash, A. Bronnikov, O. Zharikov, and A. Pal'nichenko, Superconductivity of graphite intercalation compound with lithium C_2Li, Solid State Commun. **69**, 921 (1989).

[13] I. Belash, A. Bronnikov, O. Zharikov, and A. Palnichenko, On the superconductivity of graphite intercalation compounds with sodium, Solid State Commun. **64**, 1445 (1987).

[14] A. Gauzzi, S. Takashima, N. Takeshita, C. Terakura, H. Takagi, N. Emery, C. Hérold, P. Lagrange, and G. Loupias, Enhancement of superconductivity and evidence of structural instability in intercalated graphite C_6Ca under high pressure, Phys. Rev. Lett. **98**, 067002 (2007).

[15] C.-M. Hao, X. Li, A. R. Oganov, J. Hou, S. Ding, Y. Ge, L. Wang, X. Dong, H.-T. Wang, G. Yang, X.-F. Zhou, and Y. Tian, Superconductivity in compounds of sodium-intercalated graphite, Phys. Rev. B **108**, 214507 (2023).

[16] W. L. McMillan, Transition temperature of strong-coupled superconductors, Phys. Rev. **167**, 331 (1968).

[17] P. B. Allen and R. C. Dynes, Transition temperature of strong-coupled superconductors reanalyzed, Phys. Rev. B **12**, 905 (1975).

[18] A. R. Oganov, *Modern Methods of Crystal Structure Prediction* (John Wiley & Sons, Weinheim, Germany, 2011).

[19] A. R. Oganov, C. J. Pickard, Q. Zhu, and R. J. Needs, Structure prediction drives materials discovery, Nat Rev Mater **4**, 331 (2019).

[20] Y. Wang and Y. Ma, Perspective: Crystal structure prediction at high pressures, J. Chem. Phys. **140**, 040901 (2014).

[21] L. Boeri *et al.*, The 2021 room-temperature superconductivity roadmap, J. Phys.: Condens. Matter **34**, 183002 (2022).

[22] A. N. Kolmogorov, S. Shah, E. R. Margine, A. F. Bialon, T. Hammerschmidt, and R. Drautz, New superconducting and semiconducting Fe-B compounds predicted with an *ab initio* evolutionary search, Phys. Rev. Lett. **105**, 217003 (2010).

[23] A. N. Kolmogorov, S. Shah, E. R. Margine, A. K. Kleppe, and A. P. Jephcoat, Pressure-driven evolution of the covalent network in CaB_6, Phys. Rev. Lett. **109**, 075501 (2012).

[24] S. Hajinazar, A. Thorn, E. D. Sandoval, S. Kharabadze, and A. N. Kolmogorov, MAISE: Construction of neural network interatomic models and evolutionary structure optimization, Comput. Phys. Commun. **259**, 107679 (2021).

[25] S. Shah and A. N. Kolmogorov, Stability and superconductivity of Ca-B phases at ambient and high pressure, Phys. Rev. B **88**, 014107 (2013).

[26] S. Kharabadze, A. Thorn, E. A. Koulakova, and A. N. Kolmogorov, Prediction of stable Li-Sn compounds: Boosting *ab initio* searches with neural network potentials, npj Comput Mater **8**, 136 (2022).

[27] J. Singh, A. Behatha, S. Kharabadze, A. N. Kolmogorov, G. Vaitheeswaran, and V. Kanchana, Prediction of ground state structures and robust Weyl fermionic states in MnRhP, J. Phys. Chem. C **126**, 17328 (2022).

[28] S. Kharabadze, M. Meyers, C. R. Tomassetti, E. R. Margine, I. I. Mazin, and A. N. Kolmogorov, Thermodynamic stability of Li–B–C compounds from first principles, Phys. Chem. Chem. Phys. **25**, 7344 (2023).

[29] C. R. Tomassetti, G. P. Kafle, E. T. Marcial, E. R. Margine, and A. N. Kolmogorov, Prospect of high-temperature superconductivity in layered metal borocarbides, J. Mater. Chem. C **12**, 4870 (2024).

[30] K. Momma and F. Izumi, *VESTA3* for three-dimensional visualization of crystal, volumetric and morphology data, J. Appl. Cryst. **44**, 1272 (2011).

[31] J. Klimeš, D. R. Bowler, and A. Michaelides, Chemical accuracy for the van der Waals density functional, J. Phys.: Condens. Matter **22**, 022201 (2010).

[32] J. Klimeš, D. R. Bowler, and A. Michaelides, Van der waals density functionals applied to solids, Phys. Rev. B **83**, 195131 (2011).

[33] E. R. Margine and F. Giustino, Anisotropic Migdal-Eliashberg theory using Wannier functions, Phys. Rev. B **87**, 024505 (2013).

[34] H. Lee, S. Poncé, K. Bushick, S. Hajinazar, J. Lafuente-Bartolome, J. Leveillee, C. Lian, J.-M. Lihm, F. Macheda, H. Mori, H. Paudyal, W. H. Sio, S. Tiwari, M. Zacharias, X. Zhang, N. Bonini, E. Kioupakis, E. R. Margine, and F. Giustino, Electron–phonon physics from first principles using the EPW code, npj Comput. Mater. **9**, 2057 (2023).

[35] R. Lucrezi, P. P. Ferreira, S. Hajinazar, H. Mori, H. Paudyal, E. R. Margine, and C. Heil, Full-bandwidth anisotropic Migdal-Eliashberg theory and its application to superhydrides, Commun. Phys. **7**, 33 (2024).

[36] A. Y. Liu, I. I. Mazin, and J. Kortus, Beyond Eliashberg superconductivity in MgB_2: Anharmonicity, two-phonon scattering, and multiple gaps, Phys. Rev. Lett. **87**, 087005 (2001).

[37] H. J. Choi, D. Roundy, H. Sun, M. L. Cohen, and S. G. Louie, The origin of the anomalous superconducting properties of MgB_2, Nature (London) **418**, 758 (2002).

[38] H. J. Choi, S. G. Louie, and M. L. Cohen, Prediction of superconducting properties of CaB_2 using anisotropic Eliashberg theory, Phys. Rev. B **80**, 064503 (2009).

[39] G. P. Kafle, C. R. Tomassetti, I. I. Mazin, A. N. Kolmogorov, and E. R. Margine, *Ab initio* study of Li-Mg-B superconductors, Phys. Rev. Mater. **6**, 084801 (2022).

[40] J. Wang, M. Wang, X. Liu, M. Jiang, and L. Liu, Covalent bond inducing strong electron-phonon coupling superconductivity in MgB_2-type transition metal diboride WB_2, Phys. Rev. Mater. **7**, 074804 (2023).

[41] C. R. Tomassetti, D. Gochitashvili, C. Renskers, E. R. Margine, and A. N. Kolmogorov, First-principles design of ambient-pressure $Mg_xB_2C_2$ and Na_xBC superconductors, arXiv:2407.09347 [Phys. Rev. M (to be published)].

[42] G. Kresse and J. Furthmüller, Efficient iterative schemes for *ab initio* total-energy calculations using a plane-wave basis set, Phys. Rev. B **54**, 11169 (1996).

[43] P. E. Blöchl, Projector augmented-wave method, Phys. Rev. B **50**, 17953 (1994).

[44] J. W. Furness, A. D. Kaplan, J. Ning, J. P. Perdew, and J. Sun, Accurate and numerically efficient r^2 SCAN meta-generalized gradient approximation, J. Phys. Chem. Lett. **11**, 8208 (2020).

[45] J. Ning, M. Kothakonda, J. W. Furness, A. D. Kaplan, S. Ehlert, J. G. Brandenburg, J. P. Perdew, and J. Sun, Workhorse minimally empirical dispersion-corrected density functional with tests for weakly bound systems: r^2 SCAN+rVV10, Phys. Rev. B **106**, 075422 (2022).

[46] A. Togo and I. Tanaka, First principles phonon calculations in materials science, Scr. Mater. **108**, 1 (2015).

[47] See Supplemental Material at http://link.aps.org/supplemental/10.1103/PhysRevB.110.174508 for additional figures and structural information. Figures S1 and S2 illustrate the distance to the convex hull for select Na-C phases using the optB86b-vdW and optB88-vdW functionals. Figure S3 presents the stability analysis using the r^2SCAN + rVV10 functional. Figure S4 shows the enthalpy-pressure curves for select stable structures. Figures S5-S7 display the phonon dispersion of oS52-Na_3C_{10} (*Cmcm*), oS52-Na_3C_{10} ($C222_1$), and oP104-Na_3C_{10} calculated using PHONOPY and VASP. Figure S8 illustrates the electronic structure, phonon dispersion, and Eliashberg spectra function of oP104-Na_3C_{10} calculated using Quantum ESPRESSO. Figures S9-S12 detail oS20-NaC_4 properties: the orbital-projected electronic structure, DOS, Fermi surface, phonon dispersion, PhDOS, $\alpha^2F(\omega)$, and e-ph coupling. Full structural information for select Na-C phases is given in CIF format.

[48] P. Giannozzi *et al.*, Advanced capabilities for materials modelling with Quantum ESPRESSO, J. Phys.: Condens. Matter **29**, 465901 (2017).

[49] T. Thonhauser, S. Zuluaga, C. A. Arter, K. Berland, E. Schröder, and P. Hyldgaard, Spin signature of nonlocal correlation binding in metal-organic frameworks, Phys. Rev. Lett. **115**, 136402 (2015).

[50] K. Berland, V. R. Cooper, K. Lee, E. Schröder, T. Thonhauser, P. Hyldgaard, and B. I. Lundqvist, van der Waals forces in density functional theory: A review of the vdW-DF method, Rep. Prog. Phys. **78**, 066501 (2015).

[51] D. R. Hamann, Optimized norm-conserving Vanderbilt pseudopotentials, Phys. Rev. B **88**, 085117 (2013).

[52] M. van Setten, M. Giantomassi, E. Bousquet, M. Verstraete, D. Hamann, X. Gonze, and G.-M. Rignanese, The PseudoDojo: Training and grading a 85 element optimized norm-conserving pseudopotential table, Comput. Phys. Commun. **226**, 39 (2018).

[53] J. P. Perdew, K. Burke, and M. Ernzerhof, Generalized gradient approximation made simple, Phys. Rev. Lett. **77**, 3865 (1996).

[54] M. Methfessel and A. T. Paxton, High-precision sampling for Brillouin-zone integration in metals, Phys. Rev. B **40**, 3616 (1989).

[55] S. Baroni, S. de Gironcoli, A. Dal Corso, and P. Giannozzi, Phonons and related crystal properties from density-functional perturbation theory, Rev. Mod. Phys. **73**, 515 (2001).

[56] F. Giustino, M. L. Cohen, and S. G. Louie, Electron-phonon interaction using Wannier functions, Phys. Rev. B **76**, 165108 (2007).

[57] S. Poncé, E. Margine, C. Verdi, and F. Giustino, EPW: Electron–phonon coupling, transport and superconducting properties using maximally localized Wannier functions, Comput. Phys. Commun. **209**, 116 (2016).

[58] N. Marzari, A. A. Mostofi, J. R. Yates, I. Souza, and D. Vanderbilt, Maximally localized Wannier functions: Theory and applications, Rev. Mod. Phys. **84**, 1419 (2012).

[59] G. Pizzi *et al.*, Wannier90 as a community code: New features and applications, J. Phys.: Condens. Matter **32**, 165902 (2020).

[60] A. Marrazzo, S. Beck, E. R. Margine, N. Marzari, A. A. Mostofi, J. Qiao, I. Souza, S. S. Tsirkin, J. R. Yates, and G. Pizzi, The wannier-functions software ecosystem for materials simulations, arXiv:2312.10769 [Rev. Mod. Phys. (to be published)].

[61] B. Sundqvist, Carbon under pressure, Phys. Rep. **909**, 1 (2021).

[62] I. Pallikara, P. Kayastha, J. M. Skelton, and L. D. Whalley, The physical significance of imaginary phonon modes in crystals, Electron. Struct. **4**, 033002 (2022).

[63] E. D. Sandoval, S. Hajinazar, and A. N. Kolmogorov, Stability of two-dimensional BN-Si structures, Phys. Rev. B **94**, 094105 (2016).

[64] C. Lin, S. Poncé, and N. Marzari, General invariance and equilibrium conditions for lattice dynamics in 1D, 2D, and 3D materials, npj Comput. Mater. **8**, 236 (2022).

[65] C. Heil, S. Poncé, H. Lambert, M. Schlipf, E. R. Margine, and F. Giustino, Origin of superconductivity and latent charge density wave in NbS_2, Phys. Rev. Lett. **119**, 087003 (2017).

[66] J. Ying, H. Paudyal, C. Heil, X.-J. Chen, V. V. Struzhkin, and E. R. Margine, Unusual pressure-induced periodic lattice distortion in $SnSe_2$, Phys. Rev. Lett. **121**, 027003 (2018).

[67] L. Monacelli, R. Bianco, M. Cherubini, M. Calandra, I. Errea, and F. Mauri, The stochastic self-consistent harmonic approximation: Calculating vibrational properties of materials with full quantum and anharmonic effects, J. Phys.: Condens. Matter **33**, 363001 (2021).

[68] M. Zacharias, G. Volonakis, F. Giustino, and J. Even, Anharmonic lattice dynamics via the special displacement method, Phys. Rev. B **108**, 035155 (2023).

[69] R. Lucrezi, P. P. Ferreira, M. Aichhorn, and C. Heil, Temperature and quantum anharmonic lattice effects on stability and superconductivity in lutetium trihydride, Nat. Commun. **15**, 441 (2024).

[70] M.-C. Jiang, R. Masuki, G.-Y. Guo, and R. Arita, *Ab initio* study on magnetism suppression, anharmonicity, rattling mode, and superconductivity in Sc_6MTe_2(M = Fe, Co, Ni), Phys. Rev. B **110**, 104505 (2024).

[71] A. N. Kolmogorov and V. H. Crespi, Registry-dependent interlayer potential for graphitic systems, Phys. Rev. B **71**, 235415 (2005).

[72] A. N. Kolmogorov and V. H. Crespi, Smoothest bearings: Interlayer sliding in multiwalled carbon nanotubes, Phys. Rev. Lett. **85**, 4727 (2000).

[73] A. N. Kolmogorov, V. H. Crespi, M. H. Schleier-Smith, and J. C. Ellenbogen, Nanotube-substrate interactions: Distinguishing carbon nanotubes by the helical angle, Phys. Rev. Lett. **92**, 085503 (2004).

[74] A. N. Kolmogorov and S. Curtarolo, Prediction of different crystal structure phases in metal borides: A lithium monoboride analog to MgB_2, Phys. Rev. B **73**, 180501(R) (2006).

[75] A. N. Kolmogorov and S. Curtarolo, Theoretical study of metal borides stability, Phys. Rev. B **74**, 224507 (2006).

[76] A. N. Kolmogorov, S. Hajinazar, C. Angyal, V. L. Kuznetsov, and A. P. Jephcoat, Synthesis of a predicted layered LiB via cold compression, Phys. Rev. B **92**, 144110 (2015).

[77] M. Calandra and F. Mauri, Theoretical explanation of superconductivity in C_6Ca, Phys. Rev. Lett. **95**, 237002 (2005).

[78] G. Csányi, P. B. Littlewood, A. H. Nevidomskyy, C. J. Pickard, and B. D. Simons, The role of the interlayer state in the electronic structure of superconducting graphite intercalated compounds, Nat. Phys. **1**, 42 (2005).

[79] I. I. Mazin, Intercalant-driven superconductivity in YbC_6 and CaC_6, Phys. Rev. Lett. **95**, 227001 (2005).

[80] I. Mazin and A. Balatsky, Superconductivity in Ca-intercalated bilayer graphene, Philos. Mag. Lett. **90**, 731 (2010).

[81] E. Margine, H. Lambert, and F. Giustino, Electron-phonon interaction and pairing mechanism in superconducting Ca-intercalated bilayer graphene, Sci. Rep. **6**, 21414 (2016).

[82] G. Profeta, M. Calandra, and F. Mauri, Phonon-mediated superconductivity in graphene by lithium deposition, Nat. Phys. **8**, 131 (2012).

[83] J.-J. Zheng and E. R. Margine, First-principles calculations of the superconducting properties in Li-decorated monolayer graphene within the anisotropic Migdal-Eliashberg formalism, Phys. Rev. B **94**, 064509 (2016).

[84] M. Calandra, A. N. Kolmogorov, and S. Curtarolo, Search for high T_c in layered structures: The case of LiB, Phys. Rev. B **75**, 144506 (2007).

[85] L. Boeri, G. B. Bachelet, M. Giantomassi, and O. K. Andersen, Electron-phonon interaction in graphite intercalation compounds, Phys. Rev. B **76**, 064510 (2007).

[86] E. R. Margine and V. H. Crespi, Universal behavior of nearly free electron states in carbon nanotubes, Phys. Rev. Lett. **96**, 196803 (2006).

[87] A. Sanna, G. Profeta, A. Floris, A. Marini, E. K. U. Gross, and S. Massidda, Anisotropic gap of superconducting CaC_6: A first-principles density functional calculation, Phys. Rev. B **75**, 020511(R) (2007).

[88] M. Calandra and F. Mauri, Possibility of superconductivity in graphite intercalated with alkaline earths investigated with density functional theory, Phys. Rev. B **74**, 094507 (2006).

[89] A. Sanna, S. Pittalis, J. K. Dewhurst, M. Monni, S. Sharma, G. Ummarino, S. Massidda, and E. K. U. Gross, Phononic self-energy effects and superconductivity in CaC_6, Phys. Rev. B **85**, 184514 (2012).

[90] P. P. Ferreira, L. J. Conway, A. Cucciari, S. Di Cataldo, F. Giannessi, E. Kogler, L. T. F. Eleno, C. J. Pickard, C. Heil, and L. Boeri, Search for ambient superconductivity in the Lu-N-H system, Nat. Commun. **14** (2023).

[91] P. Tsuppayakorn-aek, P. Pluengphon, W. Sukmas, A. Sakulkalavek, B. Inceesungvorn, W. Luo, and T. Bovornratanaraks, Role of anharmonicity in phonon-mediated superconductivity of quasi- van der Waals layered XP_2 (X = As, Sb, Bi) structures: Insight from first-principles calculations, J. Alloys Compd. **959**, 170440 (2023).

[92] M. Kawamura, FermiSurfer: Fermi-surface viewer providing multiple representation schemes, Comput. Phys. Commun. **239**, 197 (2019).

[93] S. Xie, Y. Quan, A. Hire, B. Deng, J. DeStefano, I. Salinas, U. Shah, L. Fanfarillo, J. Lim, J. Kim *et al.*, Machine learning of superconducting critical temperature from Eliashberg theory, npj Comput. Mater. **8**, 14 (2022).

[94] W. Sano, T. Koretsune, T. Tadano, R. Akashi, and R. Arita, Effect of van Hove singularities on high-T_c superconductivity in H_3S, Phys. Rev. B **93**, 094525 (2016).

[95] Y. Quan and W. E. Pickett, Van Hove singularities and spectral smearing in high-temperature superconducting H_3S, Phys. Rev. B **93**, 104526 (2016).

[96] D. Stanzione, J. West, R. T. Evans, T. Minyard, O. Ghattas, and D. K. Panda, Frontera: The evolution of leadership computing at the national science foundation, in *Practice and Experience in Advanced Research Computing* (ACM, New York, NY, USA, 2020), pp. 106–111.

[97] T. J. Boerner, S. Deems, T. R. Furlani, S. L. Knuth, and J. Towns, ACCESS: Advancing innovation: NSF's advanced cyberinfrastructure coordination ecosystem: Services & Support, in *Practice and Experience in Advanced Research Computing*, PEARC '23 (Association for Computing Machinery, New York, NY, USA, 2023), pp. 173–176.